Investigation of Shock Configurations Induced by a Plume Impinging upon a Perpendicular Plate

Irina A. Graur[1], Tatiana G. Elizarova[1], and Jean-Claude Lengrand[2]

[1] Institute of Mathematical Modeling, Russian Academy of Science, Miusskaya sq. 4a, 125047 Moscow, Russia
[2] Laboratoire d'Aérothermique du CNRS, 1C av. de la Recherche Scientifique, 45071 Orléans Cedex 2, France

Abstract. The present work is an investigation of the normal impingement of an underexpanded jet upon a plane surface for different external pressures. Computations were carried out based on the quasigasdynamic equations and compared with the experimental results obtained in the SR3 low-density facility of the laboratoire d'Aérothermique.

1 Introduction

Jets issued from satellite control thrusters or from stage separation retro-rockets may impinge upon spacecraft walls, antennas or solar arrays, causing dynamic and thermal loads. In the particular case of normal impingement, those effects depend strongly upon the configuration of the shocks induced both by the surface and by the external atmosphere, if any. A numerical simulation of a jet impinging upon a perpendicular surface has been considered for the operating conditions of experiments that were carried out in the SR3 low-density facility.

Nitrogen plumes were issued from a 10° half-angle conical nozzle with stagnation temperatures $T_0 = 600$ K (variant A) and $1100\,$K (variant B) and stagnation pressures $p_0 = 0.5$ bar (see Table 1). The background pressure p_∞ was varied in the range from 8 to 330 Pa. Two flat plates were designed for pressure and heat transfer measurement, respectively and located at a distance $z_{max} = 40\, r_e = 0.1644\,$m from the nozzle, were r_e is the nozzle exit radius. It was found [1] that for low values of the background pressures $p_\infty = 8, 16, 33\,$Pa, the shock induced ahead of the plate intersected the jet axis within the first expansion cell. For higher values of p_∞ the central part of the plate was downstream of the plume first recompression wave.

2 Quasigasdynamic Equations

The numerical interpretation is based on the quasigasdynamic (QGD) system of equations. Theoretical investigation and numerical implementation of QGD system are summarized in [2]. The gasdynamic system consists of three differential

Table 1. Flow parameters

Quantities	Notation	A	B
Nozzle exit pressure	p_e (Pa)	1612	1654
Nozzle exit temperature	T_e (K)	224.9	415.4
Stagnation temperature	T_0 (K)	600	1100
Nozzle exit Mach number	Ma_e	2.89	2.88
Nozzle wall temperature	T_{wn}	350	400
Knudsen number	$Kn = \lambda_e/2r_e$	$2.89 \cdot 10^{-4}$	$6.03 \cdot 10^{-4}$

equations accounting for conservation of mass, momentum and total energy

$$\frac{\partial \rho}{\partial t} + \nabla_i J^i = 0, \tag{1}$$

$$\frac{\partial (\rho u^k)}{\partial t} + \nabla_i J^i u^k + \nabla^k p = \nabla_i \Pi^{ik}, \tag{2}$$

$$\frac{\partial E}{\partial t} + \nabla_i \frac{J^i}{\rho}(E+p) + \nabla_i q^i = \nabla_i (\Pi^{ik} u^k). \tag{3}$$

To close the system (1)–(3) the mass flux vector J^i, the shear-stress tensor Π^{ik}, and the heat flux vector q^i must be expressed as a function of the macroscopic flow quantities: density ρ, velocity components u_i, and pressure p. Different choices for J^i, Π^{ik}, q^i lead either to the Navier–Stokes equations, or to the present QGD equations. Navier–Stokes equations are derived from

$$J^i_{NS} = \rho u^i, \qquad q^i_{NS} = -\kappa \nabla^i T,$$

$$\Pi^{ik}_{NS} = \mu \left(\nabla^k u^i + \nabla^i u^k - (2/3) g^{ik} \nabla_j u^j \right) + \eta g^{ik} \nabla_j u^j,$$

Here the involved gasdynamic variables ρ, u_i, and p are instantaneous space averaged quantities, and Π^{ik}_{NS} is the Navier–Stokes shear-stress tensor, g^{ik} is the metric tensor, μ and κ are the viscosity and heat conductivity coefficients, respectively, η is the second viscosity coefficient (bulk viscosity).

In contrast to the Navier–Stokes equations, if the gasdynamic quantities ρ, u_i, and p are defined by means of time-space averaging, instead of space averaging, the system (1)–(3) can be closed by other ways, in particular by

$$J^i = \rho u^i - \tau \left(\nabla_j (\rho u^i u^j) + \nabla^i p \right), \quad q^i = q^i_{NS} - \tau \rho T u^i \left(u^j \nabla_j s \right), \tag{4}$$

$$\Pi^{ik} = \Pi^{ik}_{NS} + \tau u^i \left(\rho u^j \nabla_j u^k + \nabla^k p \right) + \tau g^{ik} \left(u_j \nabla^j p + \gamma p \nabla_j u^j \right), \tag{5}$$

where $\varepsilon = p/[\rho(\gamma-1)]$ is the specific internal energy, s is the specific entropy, $\tau = \mu/p$ is the Maxwell relaxation time. Equations (1)–(3) with (4)–(5) form the QGD equations, a system where the mass, momentum, and total energy conservation laws, and the entropy theorem are valid as for the classic Navier–Stokes system. QGD equations were obtained also by a kinetical approach that consists in integrating a model kinetic equation multiplied by collisional invariants.

For slightly nonequilibrium flows the time-space averaged quantities and the space-averaged quantities are similar, QGD and Navier–Stokes systems differing by $O(\tau)$. For stationary flows, the dissipative terms (terms in τ) in the QGD equations appear as Navier–Stokes terms, QGD and Navier–Stokes equations differing by additional terms whose asymptotic order is τ^2 for $\tau \to 0$, or, in the dimensionless form of the equations, $O(Kn^2)$ for $Kn \to 0$. The boundary layer approximation for QGD equations leads to the classic Prandtl equation system.

3 Problem formulation and computational results

The problem under consideration is solved in $(r - z)$ formulation using QGD equations. The viscosity law is taken as $\mu \sim T^{\omega}$. The computational domain is shown in Fig. 1. As boundary conditions, no-slip was assumed for the left wall and for the plate (with temperature $T_w = 293\,\mathrm{K}$), usual symmetry conditions and “soft” conditions were applied on the axis and on the upper boundary, respectively. At nozzle exit, a laminar boundary layer profile was prescribed [3].

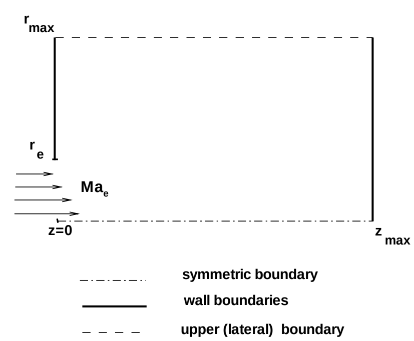

Fig. 1. Computational domain

For a solution of QGD equations the upwind-type spliting scheme was used based on the additional dissipative terms of QGD system (see [4] for details). Second-order accuracy was obtained by applying the standard MUSCL approximation and “minmod” limiter. For the diffusive terms a second-order central difference scheme was applied.

Computations were carried out for nitrogen ($\gamma = 1.4$, $\omega = 0.74$, $Pr = 0.736$), for 2 variants of flow conditions at nozzle exit (jets A and B) and for 6 values of the background pressure $p_\infty = 8, 16, 33, 66, 160$ and 330 Pa, thus reproducing the experimental conditions (Table 2). In the present paper only the variants for jet B are discussed. The results for jet A were found to be similar.

For all variants, rectangular computational grids were used with steps $h_{rmin} = 0.1\,r_e$ and $h_z = 0.25\,r_e$ (variants 1 and 2), or $h_z = 0.5r_e$ (variants 3–6). The number of steps varied from 161×115 ($r_{max} = 100r_e$) for variant 1 to 81×73 ($r_{max} = 40r_e$) for variant 6. For a solution of the QGD equations an upwind-type splitting scheme was used based on the additional dissipative terms of QGD system (see [4] for details). Second-order accuracy was obtained by applying the standard MUSCL approximation and “minmod” limiter. For the diffusive terms a second-order central difference scheme was applied.

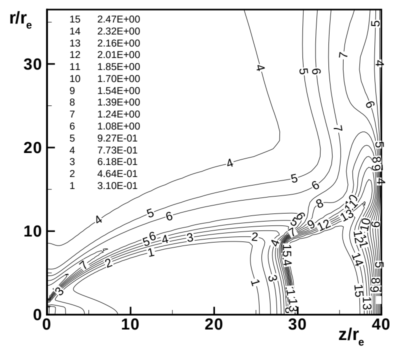

Fig. 2. Isotherms for variant 2

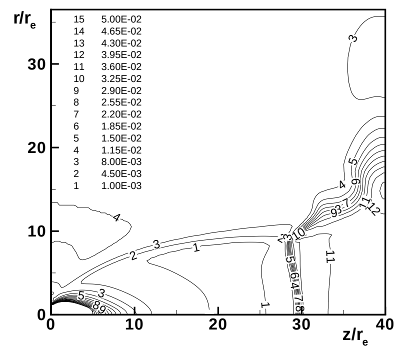

Fig. 3. Isobars for variant 2

In Table 2 is shown the extent z^c of the first expansion cell as found in numerical simulations of jet B when it interacts with the plate, together with the estimations of this quantity for a free jet, based on formulas by Abramovich (z^{AB}), Ashkenas (z^{AS}) and Lengrand (z^L). The distance from the nozzle exit to the plate is equal to $z_{max}/r_e = 40$. When the estimated extent of the first expansion cell is larger then the distance to the plate (variants 1 and 2), the flow is stationary. It was found that the steady-state solution was reached after a number of oscillations. The level of the oscillations increased with the background pressure. Here a normal shock is formed, much like a Mach reflection in a free jet MR: the local Mach number exceeds unity before the shock and it is less then unity behind the shock. The corresponding T and p distributions for variant 2 are shown in Figs. 2 and 3. For variant 3, the first expansion cell in the undisturbed jet extends close to the plate position. For this variant the same structure as for variant 2 is found , but the numerical solution is nonstationary: the shock wave position oscillates in the limits shown in Table 2. Time-dependent pressure oscillations for the point located at $r = 0$ are presented in Fig. 6. Two

Table 2. Computational results

variant	1	2	3	4	5	6
p_∞ (Pa)	8	16	33	66	160	330
z^{AB}/r_e	87.5	61.9	43.1	30.5	19.6	13.6
z^{AS}/r_e	105.9	74.9	52.2	36.9	23.7	16.5
z^L/r_e	80.8	56.0	40.0	28.0	18.0	12.6
z^c/r_e	33.5	29.5	$28.5 \sim 30.0$	32.0	20.5	15.0
reflection	MR	MR	MR	RR	RR	RR

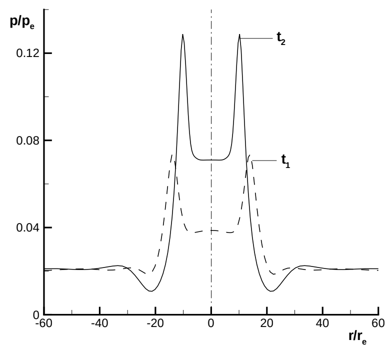

Fig. 4. Wall pressure, variant 3

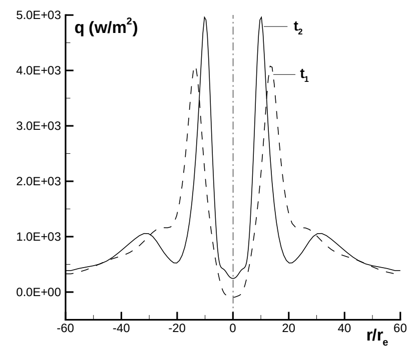

Fig. 5. Wall heat transfer, variant 3

examples of pressure $p(r)/p_e$ and heat transfer rate $q(r)$ distributions on the plate are shown in Figs. 4 and 5 for times t_1 and t_2, that correspond to the smallest t_1 and largest t_2 abscissas of the shock wave.

For variants 4, 5 and 6, the distance to the plate is larger than the extent of the first expansion cell. For variant 4, one expansion cell is formed ahead the plate, and for variant 6 two expansion cells are formed there. In these variants the flowfield remains stationary, but reflections now have a regular character (RR in Table 2): the local Mach numbers exceeds unity ahead and behind the shock wave. Isobars and isotherms for variants 4 are shown in Figs. 8 and 9. Mach number distributions along z for variants 2 (MR) and 4 (RR) are shown in Fig. 7.

The computed distributions of non-dimensionalized wall pressure p/p_e and heat transfer rate q for variants 1, 2, 4, 6 are shown in Figs. 10–13. Comparison with experimental data from [1] in the central point of the plate is given in Table

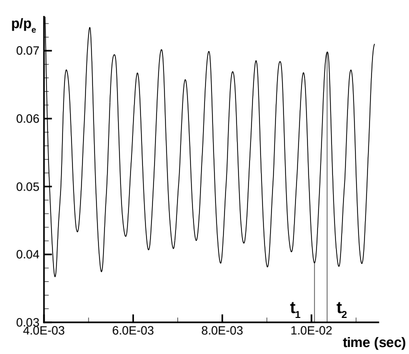

Fig. 6. Time dependent wall pressure, variant 3

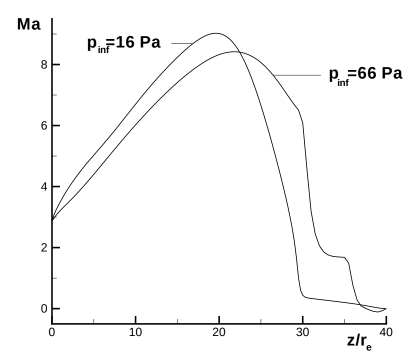

Fig. 7. Mach number distributions, variants 2 and 4

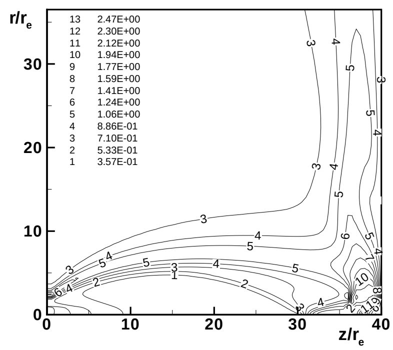

Fig. 8. Isotherms, variant 4

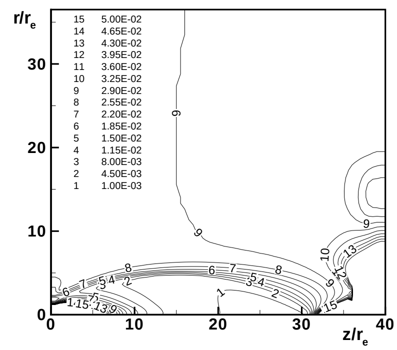

Fig. 9. Isobars, variant 4

3. Pressure profiles exhibit the same qualitative evolution as described in [1], but the calculated results appear to be slightly lower than experimental values.

Table 3. Pressure p/p_e and q [W/m^2] at the center point

variant	1	2	3	4	5	6
p_{exp}	0.038	0.048	0.068	0.7	1.2	1.9
p_{cal}	0.029	0.038	$0.039 - 0.071$	0.49	0.47	1.72
q_{exp}	$6. \cdot 10^3$	$1.2 \cdot 10^3$	$9.5 \cdot 10^2$	$4.5 \cdot 10^4$	$1.2 \cdot 10^5$	$8. \cdot 10^4$
q_{cal}	$3.1 \cdot 10^3$	$3.0 \cdot 10^3$	$-95. \sim +250$	$5.6 \cdot 10^2$	$2.5 \cdot 10^3$	$5.5 \cdot 10^3$

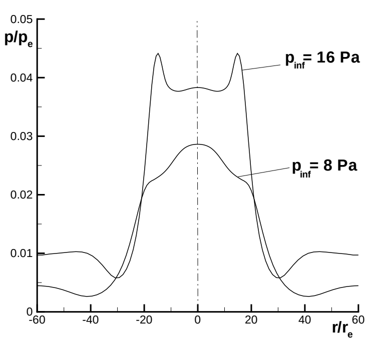

Fig. 10. Wall pressure, variants 1, 2

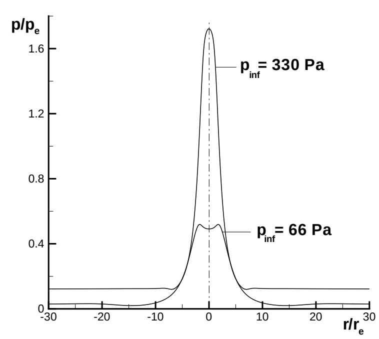

Fig. 11. Wall pressure, variants 4, 6

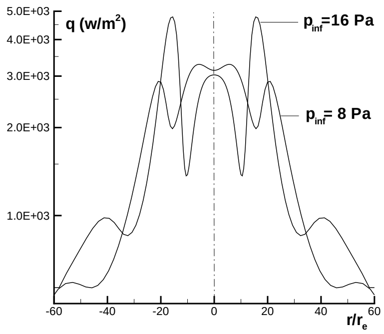

Fig. 12. Wall pressure, variants 1, 2

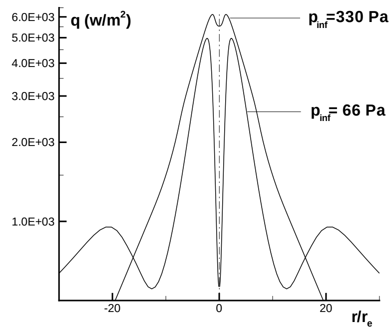

Fig. 13. Wall heat transfer, variants 4, 6

Heat transfer rates are very sensitive to the choice of computational grid and to experimental erors. They exhibit a rather complex behaviour. Nevertheless in general numerical results correspond to experimental ones. Better predictions would require finer computational grids.

4 Conclusion

Numerical results exhibit a good global agreement with experiment, and provide information on those quantities not measured in the experiment (for example, nonstationary regimes as studied in [5]).

Acknowledgement. This work was supported by Grant No. 01-01-00061 from the Russian Foundation for Basic Research.

References

1. Allègre J, Raffin M, Lengrand J.-C. (1986) Influence of background pressure on the impingement of an exhaust plume upon a perpendicular flat plate. In: Proc 15th Int Symp Rarefied Gas Dynamics, ed. by V. Boffi et al., B.G. Teubner, Stuttgart, 1:539–547
2. Elizarova TG, Sheretov YV (2001) Theoretical and numerical investigation of quasi-gasdynamic and quasihydrodynamic equations. Comput Mathem Mathem Phys 41(2):219–234
3. Graur IA, Elizarova TG, Lengrand J-C (1999) Numerical computation of shock wave configurations in underexpanded jets. Laboratoire d'Aérothermique du CNRS, Meudon, R 99-2
4. Graur IA (1999) The algorithms for the numerical solution of quasi gasdynamic equations. J Comput Mathem Mathem. Phys 33(8):1356–1371
5. Savin AV, Sokolov EI (1998) Influence of rarefaction on oscillations in an under-expanded jet impinging upon a flat plate: Numerical simulation. In: Proc 21st Int Symp Rarefied Gas Dynamics, ed. R. Brun et al., Cepadues, 623–630